Particuology 115 (2026) 390–400

Contents lists available at ScienceDirect

Particuology

journal homepage: www.elsevier.com/locate/partic

Carrier-phase DNS of iron particle cloud combustion in a highly turbulent shear layer

P. Ghofrani[a,*], T.D. Luu[b], S.H. Tey[a], O.T. Stein[b], A. Kempf[a]

[a] Chair of Fluid Dynamics, Institute for Energy and Materials Processes, University of Duisburg–Essen, Germany
[b] Engler-Bunte-Institut, Simulation of Reacting Thermo-Fluid Systems, Karlsruhe Institute of Technology, Germany

HIGHLIGHTS

- Deterministic cross-validation of CP-DNS of reactive turbulent shear layer is carried out for the first time.
- Effects of high turbulence is investigated using the most resolved CP-DNS simulation of iron particle combustion to date.
- Weak coupling observed between gas-phase turbulence and individual particle combustion.
- Turbulence primarily affects combustion through gas-phase oxygen transport rather than direct particle-gas interactions.

GRAPHICAL ABSTRACT

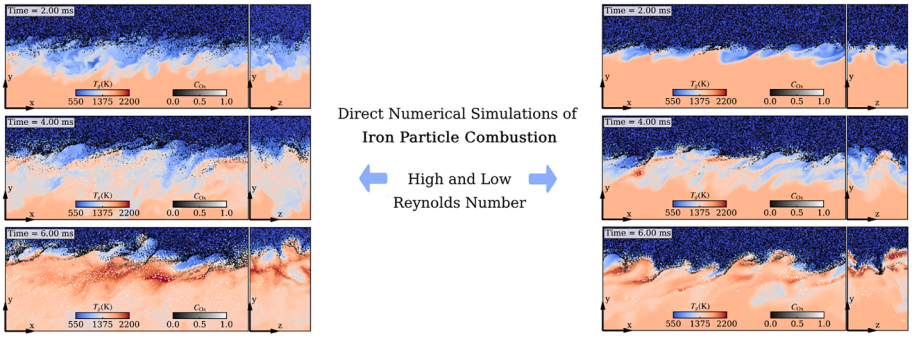

ARTICLE INFO

Keywords:
Iron combustion
Carrier-phase direct numerical simulation
Solid fuel combustion

ABSTRACT

Carrier-phase direct numerical simulations (CP-DNS) of a three-dimensional turbulent shear- and mixing-layer are presented. DNS enables detailed investigation of complex multiphase turbulent reacting systems that are difficult to study experimentally; however, the reliability and reproducibility of such simulations remain uncertain and are potentially sensitive to the underlying numerical treatment. Given this, the simulations are cross-validated against DNS data by Luu et al. (Flow Turbul. Combust. 2024), first in a statistical sense and then, for the first time, by direct comparison of the instantaneous realizations of the two DNS. A further DNS is then presented for a higher Reynolds number at twice the grid resolution. This represents the most resolved carrier-phase DNS of such systems to date and enables higher turbulence conditions that better represent realistic burner operating conditions. The new simulations confirm the previously observed overall system behavior and further demonstrate the influence of Reynolds number on the combustion process. Higher turbulence intensity leads to a broader ignition zone, enhanced oxygen entrainment, and increased ignition and conversion rates, while the particle-scale oxidation behavior remains largely unchanged, indicating weak coupling between gas-phase turbulence and individual particle combustion.

This article is part of a special issue entitled: Reactive Particle-Gas Systems II published in Particuology.

* Corresponding author.
E-mail address: parsa.ghofrani@uni-due.de (P. Ghofrani).

https://doi.org/10.1016/j.partic.2026.06.005
Received 12 January 2026; Received in revised form 15 May 2026; Accepted 1 June 2026
Available online 12 June 2026

1. Introduction

The metal-fuel cycle represents a circular energy system in which renewable electricity is used to reduce metal oxides into high-energy-density metal powders that can be transported and traded globally as a carbon-free energy carrier. During combustion for heat and power generation, the metal is reoxidized, producing solid metal oxides that can be collected and reprocessed, enabling a closed-loop system with near-zero net emissions. Among potential candidates, iron stands out due to its natural abundance, low cost, and high volumetric energy density. Furthermore, its simpler handling and transport make it a viable alternative to conventional hydrocarbon fuels, hydrogen, or ammonia for high-temperature industrial energy applications (Bergthorson et al., 2015).

Iron powder combustion involves multi-scale and multi-physics processes, including phase change, heterogeneous reactions, heat transfer, turbulence, and even nanoparticle formation. Research on single-particle combustion has provided valuable insights into ignition, combustion process and dynamics, and subsequent burn-out. Ning et al. (2021, 2022a, 2022b, 2023) experimentally investigated single iron particle combustion under various conditions. Both solid- and liquid-phase oxidation times were found to be inversely proportional to the oxygen mass fraction, suggesting that external oxygen diffusion is the rate-limiting process (Ning et al., 2023). At the same time, the characteristic burn times t_{burn} of particles of diameter d_p follow a power law, $t_{\mathrm{burn}} \propto d_p^n$, where the exponent n ranges between 1.46 and 1.72. This indicates that the overall combustion process is in an intermediate regime, not purely dictated by classical d_p^1 (kinetic) or d_p^2 (diffusion) laws. Ning et al. (2022a) also reported that the combustion process can produce a cloud of nanoparticles around the main particle if a critical particle temperature of about 2100 K is exceeded. The ignition temperatures of micron-sized iron particles have been measured in various experimental configurations by Cen (2024, 2025), Ning (2024), Panahi (2022) and their respective co-workers. Reported ignition temperatures range from 1030 K to 1130 K, with no observed dependence on particle size or oxygen level. These single-particle measurements have contributed to an understanding of the physical phenomena and the development of sub-models for cloud combustion. Hazenberg and Van Oijen (2021) were the first to introduce a numerical model for iron dust flames, derived from the more general model proposed by Soo et al. (2015). This model was subsequently improved by Thijs et al. (2022) and Mich et al. (2023), with a more accurate description of heat and mass transfer. The sub-model has been employed to numerically investigate single-particle combustion, enabling the analysis of phenomena that are challenging to measure experimentally, including nanoparticle formation (Nguyen et al., 2025; Thijs et al., 2023).

Laminar flame experiments, including iron particle clouds, were conducted in Bunsen-type burners. Julien et al. (2015) examined flame stabilization and investigated discrete and continuous propagation regimes as well as representative burning velocities for methane-iron-air suspensions, and Fedoryk et al. (2023) managed to stabilize a self-sustained iron flame. Numerical studies analyzing the laminar flame structure, stability, discreteness effects, and burning velocities were carried out by Hazenberg et al. (2026). Some groups have started to explore flame stabilization and the transition toward turbulent combustion in large lab scale burners (Steffens et al., 2025). At industrial scales, conceptual studies have highlighted the potential but also outlined the challenges of retrofitting coal power plants for iron combustion under high load conditions (Neumann et al., 2024).

Despite substantial progress on small and large scales experiments, the intermediate turbulent flame scale, and the coupling of turbulence and the combustion dynamics of iron particles, remains underexplored. A key aspect is the influence of turbulence on iron particle reactivity due to clustering and preferential concentration. Specifically, particles segregate into dense clusters and voids, potentially suppressing local oxidation rates via oxygen depletion (Krüger et al., 2017). Nevertheless, the collective heating effect caused by clustering could promote earlier ignition (Thäter et al., 2024). The complex environment of turbulent iron flames limits detailed measurements and analysis at realistic turbulent conditions, making Direct Numerical Simulations (DNS) one of the most suitable techniques for obtaining further detailed insight. Particle-resolving DNS remains computationally prohibitive and limited to single particle or small particle assemblies, as demonstrated by Thijs (2024), Vance (2023, 2025), Nguyen (2025) and their co-authors. Therefore, carrier-phase DNS (CP-DNS), which resolves the turbulent gas phase and employs a point-particle treatment with sub-models for heat and mass transfer and oxidation, provides an effective alternative for investigating multiphase dynamics in experimentally inaccessible regimes. CP-DNS has been conducted by many researchers for liquid fuels and volatile-containing solid fuels such as coal and biomass, for example by (Brosh et al., 2015; Chen et al., 2023; Hara et al., 2015; Rieth et al., 2018; Shamooni et al., 2021; Wang et al., 2021). More recently, Luu et al. (2024a, 2024b) have performed CP-DNS for iron particles, investigating the ignition and combustion in a turbulent mixing layer for mono- and polydisperse particle size distributions. They found a strong limiting effect of local oxygen concentration on the overall conversion process. Hemamalini et al. (2024) investigated the effects of preferential concentration using CP-DNS. The particle size was found to affect preferential concentration strongly, with small iron particles burning in a laminar-like regime.

In this paper, we perform a cross-validation of newly generated CP-DNS data against the reference dataset of Luu et al. (2024a), combining statistical comparisons with, to the best of our knowledge, the first deterministic one-to-one comparison of instantaneous fields obtained from two independently developed DNS codes for reacting gas–particle flows. This provides a unique assessment of reproducibility and numerical sensitivity in such simulations. Furthermore, we present the first DNS study of iron particle combustion at substantially higher Reynolds number, constituting the most highly resolved carrier-phase DNS of this class of systems to date. The grid resolution is refined by a factor of two, from $\Delta = 100$ μm to 50 μm, resulting in 680 million cells compared to 85 million in the baseline case. This enables an increase in Reynolds number by $2^{4/3}$, achieved by increasing the streamwise velocity difference from $\Delta u_x = 30.0$ m/s to 75.6 m/s. The simulations thereby allow, for the first time, the investigation of the interaction between elevated turbulence levels and mixing, ignition, and combustion behavior of iron particles, as well as characterization of the differences between low- and high-turbulence regimes. In addition, this highly resolved DNS dataset is made available to the community for further analysis and model development.

2. Modeling

The modeling framework adopted in this study is based on established approaches for solid fuel combustion (Luu et al., 2024a, 2024b; Rieth et al., 2018), with relevant concepts adapted where appropriate.

2.1. Gas phase

The gas phase is described in a Eulerian framework by the conservation equations for mass, momentum, total enthalpy, and species mass fractions, including additional source terms for inter-phase coupling:

$$\frac{\partial \rho}{\partial t} + \frac{\partial (\rho u_i)}{\partial x_i} = \dot{S}_{\rho,p} \tag{1}$$

$$\frac{\partial (\rho u_i)}{\partial t} + \frac{\partial \left(\rho u_i u_j\right)}{\partial x_j} = -\frac{\partial p}{\partial x_i} + \frac{\partial}{\partial x_j}\left(\mu\left(\frac{\partial u_i}{\partial x_j} + \frac{\partial u_j}{\partial x_i}\right) - \frac{2}{3}\mu \frac{\partial u_k}{\partial x_k}\delta_{ij}\right) + \dot{S}_{u,p} \tag{2}$$

$$\frac{\partial (\rho Y_\alpha)}{\partial t} + \frac{\partial (\rho u_i Y_\alpha)}{\partial x_i} = \frac{\partial}{\partial x_i}\left(\frac{\mu}{\mathrm{Sc}} \frac{\partial Y_\alpha}{\partial x_i}\right) + \dot{S}_{\alpha,p} \tag{3}$$

$$\frac{\partial(\rho h)}{\partial t}+\frac{\partial(\rho u_j h)}{\partial x_j}=\frac{\partial}{\partial x_j}\left(\frac{\mu}{\mathrm{Pr}}\frac{\partial h}{\partial x_j}\right)+\dot{S}_{h,p} \tag{4}$$

These equations feature the velocity vector u_i, density ρ, pressure p, total enthalpy h, and species mass fraction Y_α, where α here is oxygen. The viscosity μ of the gas phase is calculated from kinetic gas theory, and the Schmidt and Prandtl numbers are constant (Pr = Sc = 0.7). The source terms $\dot{S}_{*,p}$ represent particle-gas interactions and are defined in the following section.

2.2. Particle phase

The iron particles are modeled in a Lagrangian framework as spherical particles driven solely by drag force F_{drag}. The particle temperature T_p is considered uniform and affected by convective heat exchange, radiation, and heat of combustion. With interpolated gas-phase quantities u_g and T_g at particle position, and particle mass m_p and heat capacity c_p the particle momentum and energy balances read:

$$\frac{du_p}{dt}=\frac{F_{\mathrm{drag}}}{m_p}=\frac{u_g-u_p}{\tau_p} \tag{5}$$

$$m_p c_p\frac{dT_p}{dt}=h_{\mathrm{con}}A_p\left(T_g-T_p\right)+\epsilon_p\sigma A_p\left(T_{\mathrm{rad}}^4-T_p^4\right)+\dot{Q}_c+\frac{dm_p}{dt}h_{s,O_2} \tag{6}$$

The particle momentum relaxation time τ_p is calculated using particle density ρ_p, Reynolds number Re_p and film viscosity μ_f following:

$$\tau_p=\frac{\rho_p d_p^2}{18\mu_f}\frac{1}{1+0.15\mathrm{Re}_p^{2/3}} \tag{7}$$

The convective heat transfer coefficient h_{con} is evaluated from the Ranz and Marshall (1952) correlations:

$$\mathrm{Nu}=\frac{h_{\mathrm{con}}d_p}{\lambda_f}=2+0.552\mathrm{Re}_p^{1/2}\,\mathrm{Pr}^{1/3} \tag{8}$$

Nu and λ_f are Nusselt number and film thermal conductivity, respectively. The heat source terms $\dot{Q}_c$ and $\frac{dm_p}{dt}h_{s,O_2}$ in Eq. (6) represent the heat of combustion and the added enthalpy of oxygen both given by the oxidation sub-model proposed by Mich et al. (2023). A constant radiative background temperature of $T_{\mathrm{rad}}=300K$ is also considered in Eq. (6). Thereby, iron particles are oxidized to FeO following the heterogeneous reaction $2Fe+O_2\longrightarrow 2FeO$. Only FeO is considered here as the relevant oxide at high combustion temperatures, while other oxides Fe_3O_4 and Fe_2O_3 are neglected since the oxidation happens mostly in liquid phase where only FeO phase is stable. Further oxidation occurs at lower temperatures, outside the flame zone, and is expected to mainly affect the colder post flame zone. The rate of change of particle mass can therefore be calculated from the particle diffusive area $A_d=A_p$, oxygen mass fraction Y_{O_2}, film density ρ_f, and external diffusion coefficient k_d according to:

$$\frac{dm_p}{dt}=\rho_f Y_{O_2}A_d k_d Da^* \tag{9}$$

The external diffusion coefficient k_d is evaluated from Sherwood number Sh and diffusivity of oxygen $D_{O_2,f}$ as:

$$\mathrm{Sh}=\frac{k_d d_p}{D_{O_2,f}}=2+0.552\mathrm{Re}_p^{1/2}\mathrm{Sc}^{1/3} \tag{10}$$

The Stefan flow corrections for transport properties were found to be insignificant and hence neglected.

The normalized Damköhler number in Eq. (9) quantifies the relation between diffusion and reaction and reads:

$$\mathrm{Da}^*=\frac{A_r k_r}{A_r k_r+A_d k_d} \tag{11}$$

The reactive area is defined as $A_r=(1-Y_{\mathrm{Fe}})A_p=\pi(1-Y_{\mathrm{Fe}})d_p^2$ where Y_{Fe} is iron mass fraction. The Arrhenius reaction rate constant k_r is given by $k_r=75.0e^{-14400/T_p}$. All film properties are calculated at film temperature $T_f=T_p+1/3(T_g-T_p)$.

The inter-phase coupling source terms for momentum $\dot{S}_{u,p}$, density $\dot{S}_{\rho,p}$, oxygen mass fraction $\dot{S}_{O_2,p}$ and enthalpy $\dot{S}_{h,p}$ are calculated as follows:

$$\dot{S}_{\rho,p}=\dot{S}_{O_2,p}=-\frac{1}{\Delta^3}\sum_i^{N_p}\frac{dm_p}{dt} \tag{12}$$

$$\dot{S}_{u,p}=-\frac{1}{\Delta^3}\sum_i^{N_p}\frac{d(m_p u_p)}{dt} \tag{13}$$

$$\dot{S}_{h,p}=-\frac{1}{\Delta^3}\sum_i^{N_p}\left(h_{\mathrm{con}}A_p\left(T_g-T_p\right)+\frac{dm_p}{dt}h_{s,O_2}\right) \tag{14}$$

Summations in Eqs. 12–14 are over all particles within each computational cell, with a volume of Δ^3.

3. Computational setup

The turbulent reacting shear- and mixing-layer setup is identical to the case by Luu et al. (2024a), which in turn was derived from the cases by O'Brien et al. (2014) and Rieth et al. (2018). The turbulent reacting mixing layer consists of an upper stream (us) of air ($Y_{O_2}=0.233, Y_{N_2}=0.767$) at $T_{\mathrm{us}}=550$ K that carries iron particles, and a lower stream (ls) of hot air at $T_{\mathrm{ls}}=1650$ K. The parallel streams have a velocity difference of Δu_x, as shown in Fig. 1.

The mixing layer in a domain of size L_x, L_y, L_z is characterized by an initial momentum thickness $\delta_{\theta,0}$, corresponding to the Reynolds number $\mathrm{Re}_{\delta_{\theta,0}}$, is defined using the upper and lower stream's kinematic viscosities $\nu_{\mathrm{ls}}, \nu_{\mathrm{us}}$ as follows:

$$\mathrm{Re}_{\delta_{\theta,0}}=\frac{\Delta u_x\delta_{\theta,0}}{0.5(\nu_{\mathrm{us}}+\nu_{\mathrm{ls}})} \tag{15}$$

Thereby, a hyperbolic tangent profile based on $\delta_{\theta,0}$ defines the initial

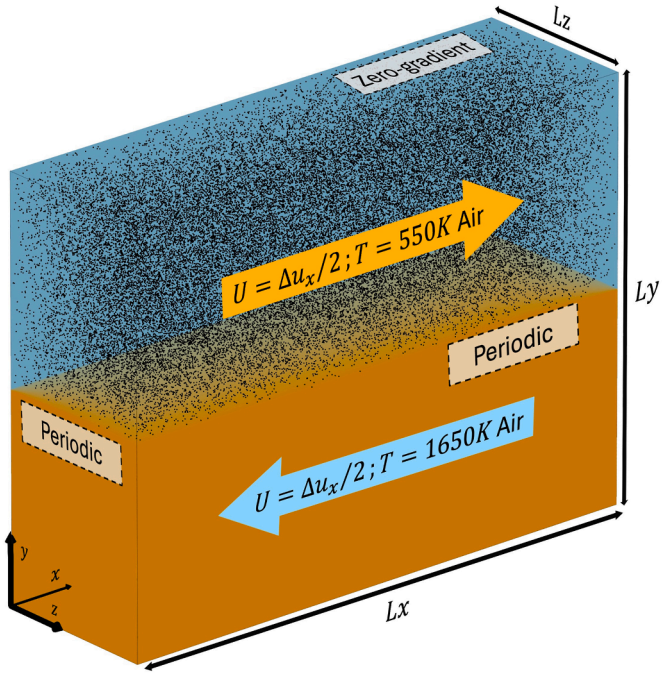

Fig. 1. Description of the initial and boundary conditions of the CP-DNS test case.

streamwise velocity field $u_{x,0} = \frac{\Delta u_x}{2}\tanh\left(\frac{y-L_y/2}{2\delta_{\theta,0}}\right)$. To accelerate the development of the mixing layer, isotropic velocity perturbations with magnitudes $\overline{u'_\beta u'_\beta} = 0.01\cdot(\Delta u_x)^2$ and a characteristic length scale of $0.01\cdot L_x$ are superimposed with the velocity fields following the approach of Klein et al. (2003) and Kempf et al. (2005).

The domain is discretized by N_{cells} cubic cells with uniform grid spacing of Δ. A total of N_p spherical pure iron particles ($Y_{\text{Fe}} = 1$), each with an initial diameter of $d_{p,\text{init}} = 10$ μm are randomly distributed in the upper stream. The number of particles is chosen to achieve an equivalence ratio of $\phi_{\text{us}} = 1$ in the upper stream. The initial particle velocities match the bulk gas velocity of the upper stream. Two cases are simulated; First, low Reynolds (*Low-Re*) case with a $\text{Re}^{\text{Low}}_{\delta_{\theta,0}}$ using an identical setup and initial fields as in Luu et al. (2024a). Second, the extended high Reynolds (*High-Re*) case with $\text{Re}^{\text{High}}_{\delta_{\theta,0}} = 2^{4/3}\cdot\text{Re}^{\text{Low}}_{\delta_{\theta,0}}$. The details of the setups are summarized in Table 1.

Periodic boundary conditions are imposed in the x- and z-directions, while a zero-gradient boundary condition is applied in the y-direction to allow fluid to leave the domain due to thermal expansion (Fig. 1). The simulations are conducted by the massively parallel in-house finite-volume DNS/LES solver *PsiPhi* (Engelmann et al., 2023; Fiorina et al., 2023; Rieth et al., 2018) in its low-Mach number version. The convective fluxes for momentum are calculated using a second-order central differencing scheme (CDS), while a total variation diminishing (TVD) scheme is adapted for scalars. The diffusive terms are discretized with second order CDS, and a third-order explicit Runge–Kutta scheme is used for time integration. The pressure Poisson-equation is solved by a preconditioned conjugate gradient solver.

4. Validation

4.1. Single particle

First, the iron particle combustion sub-model is validated by comparing single-particle predictions to experimental measurements by Ning et al. (2021) and Thijs et al. (2023), and another implementation of this sub-model (Luu et al., 2024a).

Fig. 2 illustrates the time evolution of particle temperature for a single laser-ignited iron particle of diameter $d_p = 54$ μm in air at 300 K (left), and the burn time t_{burn} of laser-ignited iron particles with different diameters burning under different oxygen concentrations at 300 K (right). The experimental data is compared to the single particle simulations. As shown, the particle temperature rises from 1500 K and then plateaus at 1810 K due to Fe melting; it subsequently peaks near 2500 K before decreasing and exhibiting another plateau at 1650 K corresponding to FeO solidification. The figure demonstrates good agreement between the current particle combustion sub-model implementation and both experimental and numerical results. Small inconsistencies between the present single particle implementation and that of Luu et al. (2024a) are likely caused by slight differences in the thermo-transport properties used in *PsiPhi* and *OpenFOAM*, as well as minor effects arising from the Stefan flow correction employed in *OpenFOAM*.

4.2. The 3D DNS–cross validation

To further verify the current CP-DNS setup and to confirm the CP-DNS results of Luu et al. (2024a) who used *OpenFOAM*, their case (*Low-Re*) was simulated again using our in-house code, *PsiPhi*, the results are compared in this section. Both simulations employed an identical computational grid, the same initial turbulent velocity fields, and an identical spatial distribution of iron particles. With perfect solvers, both simulations would yield identical results; however, in practice, they will eventually begin to deviate due to the nonlinear amplification of small differences.

Fig. 3 shows the temporal evolution of temperature, velocity, and oxygen mass fraction fields averaged in the homogeneous directions x and z. Both simulations produce nearly identical results, with small differences in the oxygen mass fraction only.

The evolution of the number of particles ignited and burnt-out, comparing results from *OpenFOAM* and *PsiPhi* is shown in Fig. 4. Ignition is defined as the time at which the particle temperature exceeds 1200 K, and burn-out corresponds to the point when the particle has fully consumed its iron mass. The ignition and burnt-out curves from both simulations agree very well throughout the simulations.

Fig. 5 illustrates the temporal evolution of the gas temperatures with particles colored by their oxidation progress C_{Ox} simulated using *PsiPhi* (left) and *OpenFOAM* (right). The particle oxidation progress $C_{\text{Ox}} = 1 - m_{\text{Fe}}/m_0$ is calculated using the initial particle mass m_0 and the mass m_{Fe} of unoxidized iron that is left in the particle, following Luu et al. (2024a, 2024b). At 2 ms, both simulations show the formation of distinct vortices that entrain the particles into the lower stream. By 4 ms, the gas temperature fields still exhibit very similar features, including streaks of hot particles entrained into the lower stream, which locally increases the gas temperature. However, as the simulation progresses further, subtle differences emerge in the structures as expected, even though the large-scale features remain largely consistent between the two codes.

The comparison shows that the two direct numerical simulations agree well. The consistency appears not only in averaged quantities and statistical measures as required, but even in the transient evolution of the results, despite the differences in the codes and the inherent sensitivity of DNS to small perturbations. This comparison demonstrates that the DNS datasets are robust, reproducible, correctly set up and not overly sensitive to the numerical schemes or codes.

The computational cost for the new simulation using *PsiPhi* was estimated to be around 20 times lower than the cost for the simulation using *OpenFOAM*, credit to the much simpler grid-structure that is used internally. This lower cost enables additional studies at a higher Reynolds number, which are presented next.

5. Results at different Reynolds number

Fig. 6 illustrates the temporal evolution of the gas temperature and particle oxidation progress C_{Ox} for the *High-Re* case. The overall features resemble those observed in the *Low-Re* case (Fig. 5), but with the expected smaller turbulent structures and a faster growth of the shear-layer thickness.

A highly turbulent mixing layer starts developing as early as 1 ms and continues growing without significant gas-phase heat-up until approximately 5 ms. During this period, particles are initially transported upward and subsequently downward by the large-scale vortical structures, while largely not following the smaller-scale turbulent motions. Several streak-like particle clusters form and become visible around 4 ms, although only a limited number of burning particles are observed. At approximately 5 ms, the first localized hot gas pocket with temperatures around 2000 K appears as a result of combustion within a particle cluster. More hot pockets subsequently form and merge, becoming increasingly pronounced by 6 ms. By 8 ms, the merging of these hot

Table 1
Summary of the simulated cases.

Case	L_x/ mm	L_y/ mm	L_z/mm	Δ/mm	N_{cells}	N_p	$Re_{\delta_{\theta,0}}$	$\delta_{\theta,0}$/ mm	Δu_x/ m s^{-1}
Low-Re	76.8	57.6	19.2	0.1	85 M	5.9 M	44	0.237	30.0
High-Re	76.8	57.6	19.2	0.05	680 M	5.9 M	111	0.237	75.6

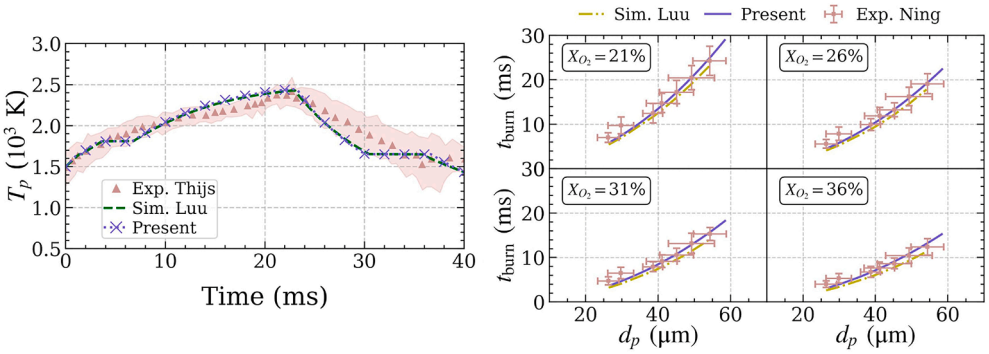

Fig. 2. Left: Evolution of particle temperature for a laser ignited iron particle of diameter $d_p = 54$ μm in 300 K air, comparing the present simulation to the Thijs et al.'s (2024) experiment and the Luu et al.'s (2024a) single particle simulations. Right: Burn time t_{burn} of laser-ignited iron particles with different diameters d_p burning under different oxygen concentrations from the present simulation compared to the experiment by Ning et al. (2021) and the simulation by Luu et al. (2024a).

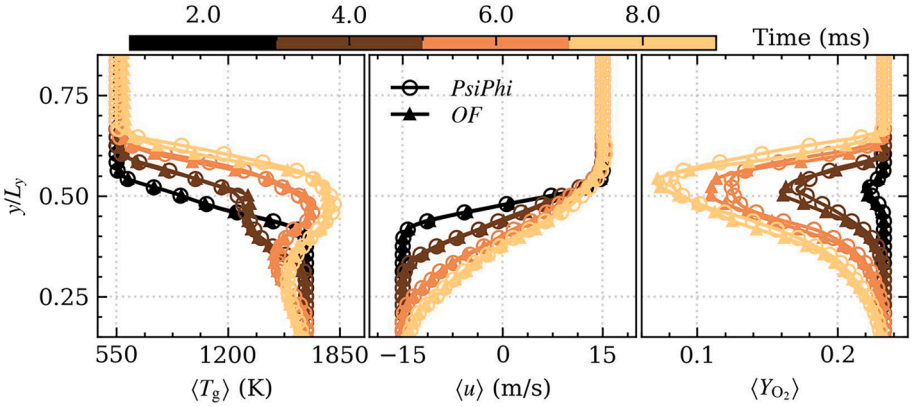

Fig. 3. Spatially-averaged gas temperature $\langle T_g \rangle$ (left), stream-wise velocity $\langle u \rangle$ (center), and oxygen mass fraction $\langle Y_{O_2} \rangle$ (bottom) from the present simulation and the work by Luu et al. (2024a).

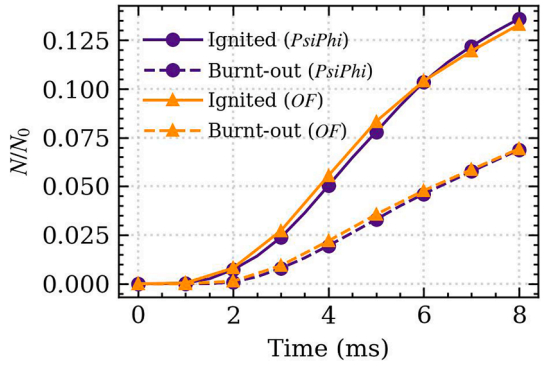

Fig. 4. Temporal evolution of the number of particles that are ignited and burnt-out from the present simulation and from the work by Luu et al. (2024a).

regions leads to the formation of a sharp interface separating hot and cold gas, as well as burnt and unburnt particles, with streaks of burning particles remaining along the interface.

Compared to the *Low-Re* case, at a higher Reynolds number, stronger turbulent mixing and broader particle dispersion is observed as expected. The enhanced mixing delays the formation of localized hot gas pockets, which appear later than in the *Low-Re* case. However, once ignition occurs, the hot regions merge more rapidly, leading to the formation of a sharp flame-like interface by 8 ms. In contrast, the low-Re case shows earlier formation of isolated hot pockets followed by a more gradual transition toward a continuous flame zone.

Fig. 7 provides scatter plots of particle oxidation progress C_{Ox} against the normalized y-coordinate y/L_y for both Reynolds numbers at different times. The marginal PDFs on the top show the spatial distribution of all and burning particles in y-direction. The particles appear to be "pushed out" of the shear layer initially, leading to increased number concentrations just below and above the shear layer. This appears to result from turbo-phoresis due to the initial, strong two-dimensional eddies that must first break up to form three-dimensional turbulence (a phenomenon that might affect flame stabilization in real burners and which we have confirmed by additional simulations with a homogeneous particle distribution throughout the domain - not shown here). In both the *Low-Re* and *High-Re* cases, oxidation is initiated near the shear layer where particles encounter intermediate gas temperatures (~1000 K). With time, the reacting region expands upwards as the mixing layer thickens, leading to ignition and higher oxidation states. By ~8 ms, the oxidation zone spans a broad range of y/L_y, with many particles approaching burnout, accompanied by elevated local gas temperatures from exothermic reactions. The spatial and temporal evolution of particle oxidation are similar between the different Reynolds numbers, with differences caused by the rate of turbulent dispersion. In *High-Re*, more particles are found at very low gas temperatures (indicated by dark points, particularly in the upper stream ($y/L_y > 0.5$) compared to the *Low-Re* case. Additionally, at comparable times, the *High-Re* case exhibits a broader temperature distribution, pointing to the presence of a differential-diffusion-like effect at the higher Reynolds number. However, the overall behavior is quite consistent between the two different Reynolds number cases.

Fig. 8 shows scatter plots of particle temperature against oxidation

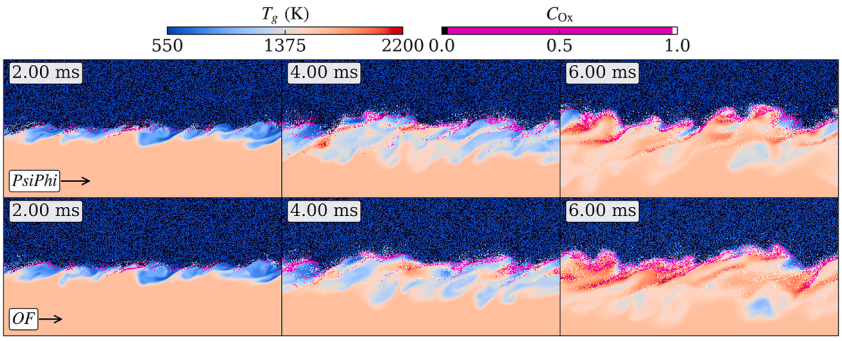

Fig. 5. Snapshots of the gas temperature in the x-y plane from the present simulation using *PsiPhi* (top row) and Luu et al.'s (2024a) simulation using *OpenFOAM* (bottom row). Particles are colored by their oxidation progress C_{Ox}.

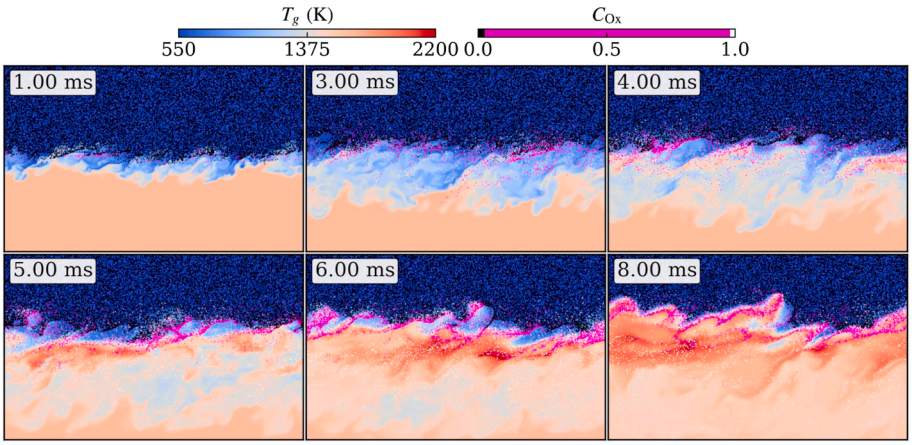

Fig. 6. Snapshots of the gas temperature and particle oxidation in the x-y plane for *High-Re* case. Particles are colored by their oxidation progress C_{Ox}. The results can also be compared with those shown in Fig. 5.

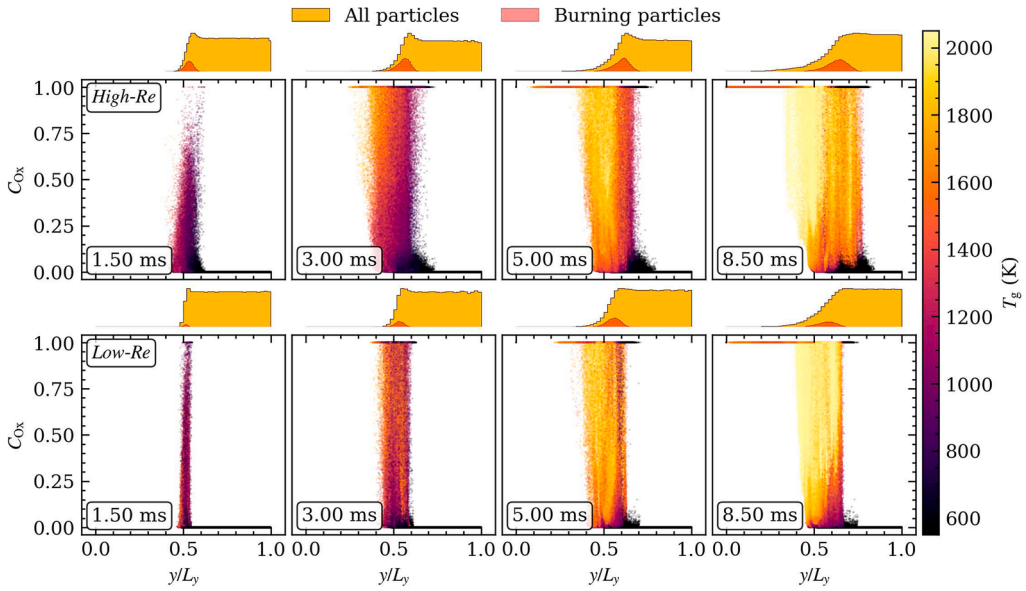

Fig. 7. Scatter plots of particle oxidation progress against normalized y coordinate, for *High-Re* (top) and *Low-Re* (bottom) cases, colored by their surrounding gas temperature at different time snapshots. The distribution of particles is shown above each sub-figure.

progress for *High-Re* and *Low-Re* cases, colored by normalized Damköhler number Da^* (Eq. (11)) at different times. Two distinct temperature plateaus are observed at 1610 K and 1810 K, corresponding to the melting and solidification of iron and iron oxide. Once particles exceed 1200 K, heterogeneous oxidation becomes diffusion-limited ($Da^* = 1$), with particles predominantly aligning along the upper temperature trajectory. As oxidation approaches completion at later times (~5–8 ms), Da^* gradually declines, particularly at lower temperatures and

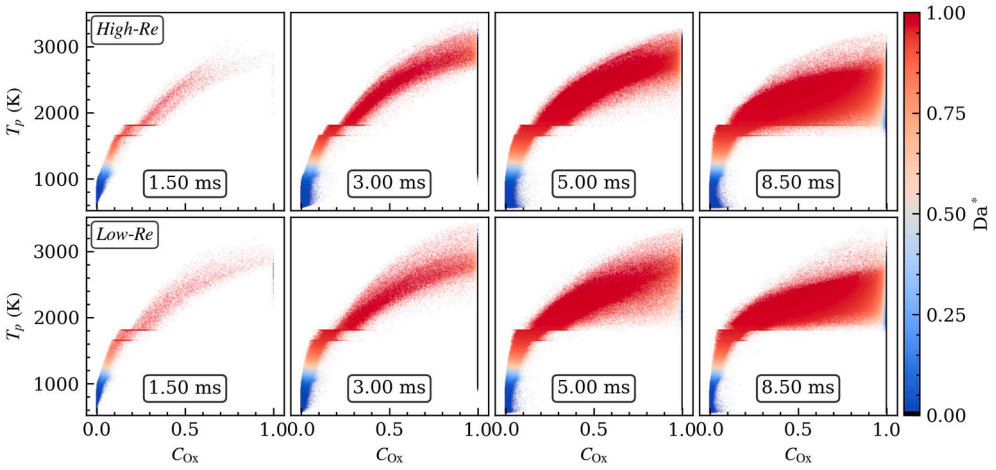

Fig. 8. Scatter plots of particle temperature against particle oxidation progress, for *High-Re* (top) and *Low-Re* (bottom) cases, colored by normalized Damköhler number Da^* (Eq. (11)), at different time snapshots.

oxidation progress, due to the limited reactive surface area. Minor differences are limited to specific instants: at 1.5 ms, the *High-Re* case shows fewer burning particles and a slight split in the oxidation trend; at ~5 ms, high turbulence exhibits a narrower temperature spread; and at ~8 ms, the *High-Re* case displays a slightly wider scatter for $C_{Ox} > 0.2$. Overall, the temporal evolution and regime transitions remain comparable between both turbulence levels.

The spatially-averaged profiles of gas-phase temperature $\langle T_g \rangle$, normalized streamwise velocity $\frac{2\langle u \rangle}{\Delta u_x}$, and oxygen mass fraction $\langle Y_{O_2} \rangle$ for *High-Re* (left) and *Low-Re* (right) cases are illustrated in Fig. 9. Overall, all the averaged profiles evolve similarly in both cases with the figures for the *High-Re* case evolving faster as a result of increased mixing and dispersion. The gas-phase temperature distribution widens as the mixing layer develops while remaining monotonic early in the simulation, showing an almost non-reactive mixing process. Subsequently, a local maximum emerges near the center of the domain at nearly 4 and 5 ms for the *Low-Re* and *High-Re* cases, respectively. This maximum is a sign of an iron flame igniting. Simultaneously, the oxygen mass fraction begins to decrease significantly, confirming the emergence of a flame. By the end of the simulation, the average temperature profile reaches a maximum of approximately 1900 K, well above the initial lower stream temperature, with the oxygen mass-fraction dropping to less than 0.1 in both cases.

Fig. 10 depicts the spatially-averaged profiles of averaged turbulent kinetic energy normalized by Δu_x^2, oxygen consumption rate, and heat exchange rate. The normalized turbulent kinetic energy increases at $y/L_y \approx 0.5$ with both a rise in magnitude and a progressive widening of the profile. It reaches a peak value of approximately 0.03 for both *Low-Re* and *High-Re* cases, after which the profiles start decreasing in magnitude while still widening. This reduction in turbulent kinetic energy is attributed to the increase in viscosity resulting from the heat release during combustion but also to the reduction in turbulence production as a result of the decaying shear rate. Throughout the domain, the *High-Re* case exhibits consistently higher turbulent kinetic energy and wider profiles than the *Low-Re* case. The oxygen consumption rate also increases while the profiles widen; however, in contrast to the turbulent kinetic energy, the peak location shifts upstream. This indicates a spatial separation between the reaction zone and the turbulent shear layer, which is expected as a result of flame propagation. As the profiles continue to widen, their magnitude decreases. The overall trend for the oxygen consumption rate profiles is similar for both Reynolds numbers. The heat exchange rate profiles are initially negative when particles are heated by the gas, before becoming positive due to the heat release of the particles and the subsequent heat transfer to the gas-phase. The negative values, indicating heating of the particles by the hotter stream, have a greater magnitude in the *High-Re* case and persist over a longer period as a result of greater particle dispersion. Later on, the heat exchange rates in both cases become positive and follow similar trends and magnitudes, with the *High-Re* case lagging behind initially before catching up and "overtaking" the *Low-Re* case. This confirms that at a higher Reynolds number, the particles can be burned more intensively and in a smaller domain, but also that a greater amount of hot (recirculating) gas is required to stabilize the combustion.

Fig. 11 (left) illustrates the temporal evolution of the normalized number of ignited and burnt-out particles (top) and their corresponding rates of change (bottom). The number of ignited particles starts increasing at approximately 2 ms, while the number of burnt-out particles begins increasing around 2.5 ms. Both cases follow a similar trend until roughly 3 ms, after which the high-Reynolds-number case exhibits consistently larger numbers of both ignited and burnt-out particles for the remainder of the simulation. The ignition rates reach peak values above 2.5 at 4 ms for the *Low-Re* case and above 5.0 at 6 ms for the *High-Re* case, before gradually leveling off at approximately 1 and 1.5, respectively. The initial high rates are because of high oxygen concentrations in the mixing layer that promotes both ignition and oxidation. Subsequently, when particle combustion causes oxygen depletion in the mixing layer the rates start decreasing and leveling off indicating flame stabilization. Fig. 11 (right) shows the temporal evolution of the total converted iron mass (top) and the iron conversion rate (bottom), normalized by the initial particle mass, for the two Reynolds numbers. The results confirm the observations from the particle-number evolution, with the *High-Re* case exhibiting consistently larger converted iron mass and faster conversion rates after approximately 3 ms. The conversion-rate curves show trends and peak locations similar to those observed for the ignition-rate evolution. This indicates that the oxidation process remains largely similar at the particle scale, while the faster overall conversion rates are primarily driven by differences in the gas-phase mixing and turbulence characteristics.

To further investigate particle scale effects, Fig. 12 examines the relationship between particle oxidation rate and the local oxygen mass fraction at the particle positions for the *High-* and *Low-Re* cases. As expected from Eq. (11), the dependence is linear, with the slope governed by the combined effects of surface reaction and external oxygen diffusion and modified by transport properties and particle slip velocity. Both cases exhibit nearly identical distributions, including similar scatter and mean slopes, as indicated by the dashed lines. This confirms that the particle-scale oxidation behavior remains largely unchanged despite differences in turbulence, indicating relatively weak coupling between turbulence and the individual particle combustion dynamics.

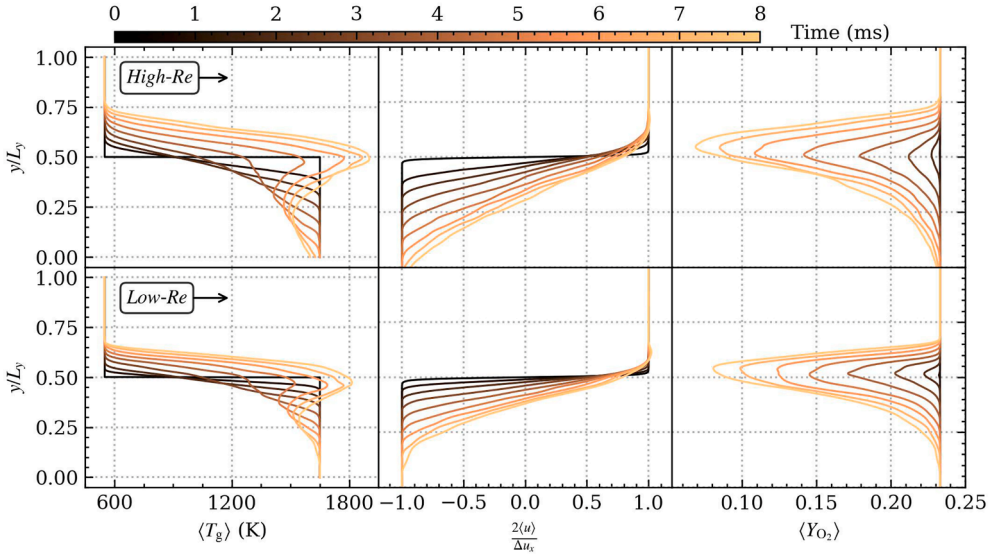

Fig. 9. Spatially-averaged gas temperature $\langle T_g \rangle$ (left), normalized stream-wise velocity $\frac{2\langle u \rangle}{\Delta u_x}$ (center), and oxygen mass fraction $\langle Y_{O_2} \rangle$ (right) for the *High-Re* (top) and *Low-Re* (bottom) cases.

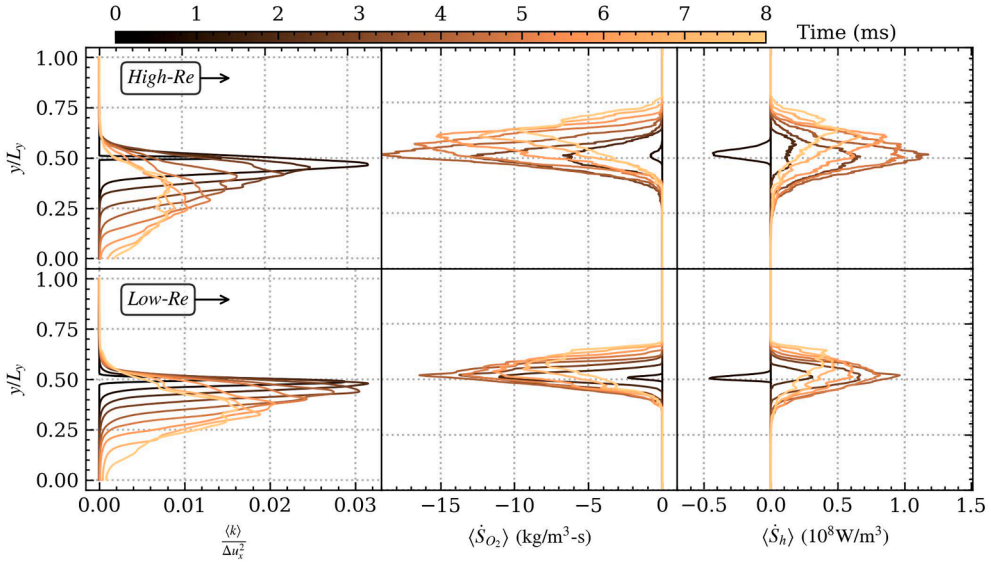

Fig. 10. Spatially-averaged normalized turbulent kinetic energy $\langle k \rangle / \Delta u_x^2$ (left), oxygen consumption rate $\langle \dot{S}_{O_2} \rangle$ (center), and heat exchange rate $\langle \dot{S}_h \rangle$ (right), comparing the *High-* (top) and *Low-Re* (bottom) cases.

Fig. 13 presents the temporal evolution of the ignited particles' mean oxidation rate normalized by the initial particle mass together with the mean oxygen mass fraction interpolated at the particle positions. Overall, both quantities decrease with time for both Reynolds numbers. Before approximately 6 ms, the *High-Re* case exhibits consistently higher mean oxidation rates, accompanied by higher local oxygen mass fractions at the particle locations. Hence, the differences in mean oxidation rates arise primarily from enhanced oxygen availability due to stronger turbulent mixing at a higher Reynolds number. Interestingly, both the mean oxygen mass fraction and the mean oxidation rate converge after approximately 6 ms. Initially, burning particles in the *High-Re* case are exposed to significantly stronger turbulence levels, as observed in Fig. 10, which enhances oxygen entrainment into the reaction zone. At later times, however, the developing spatial separation between the main reaction zone and the turbulent region reduces this effect, leading to convergence of both oxygen availability and particle oxidation rates between the two cases.

Fig. 14 illustrates the distribution of particle burn-time t_{burn} for *High-Re* and *Low-Re* conditions, where burn time t_{burn} is defined as the duration from particle ignition to burn-out. The number is normalized by the initial total number of particles. The dashed line shows the mean values for each case. The distributions of burn-times are similar; mostly between 0 and 2 ms with some particles having burn times up to 6 ms. The *High-Re* case exhibits a slightly lower mean burn time. Additionally, the *Low-Re* case shows a broader distribution with burn-time extending to roughly 6 ms. The higher burn time values in the lower Reynolds number case result from lower oxygen availability, which explains the differences in burn-out rates observed in Fig. 11.

6. Conclusion

This study investigated the combustion dynamics of iron particles within a turbulent mixing layer using carrier-phase DNS simulations. The single particle combustion model was validated by comparing

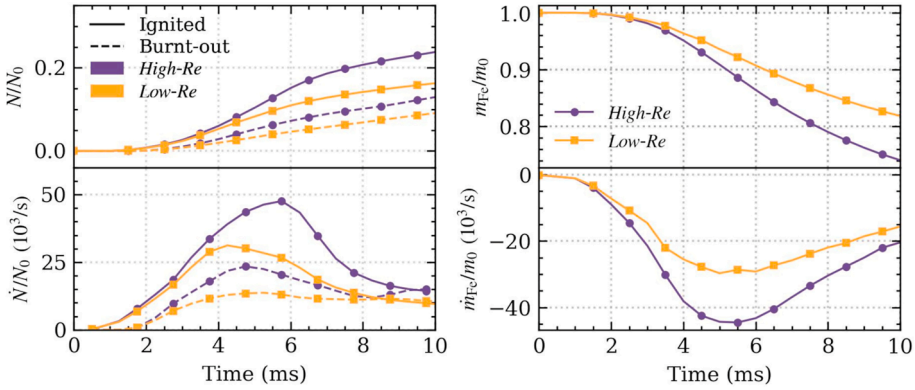

Fig. 11. Time evolution of the number of particles ignited and burnt-out (top left) and their time derivatives (bottom left) for the *High-Re* and *Low-Re* cases, normalized by the total number of particles. Time evolution of total mass of Fe (top right) and the rate of Fe conversion (bottom right) normalized by the initial total mass of particles, comparing the two cases.

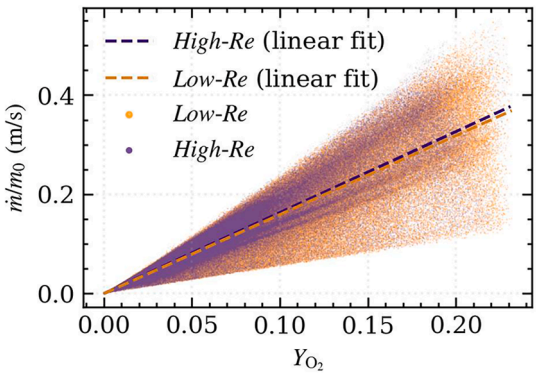

Fig. 12. Scatter plot of particle oxidation rate normalized by their initial mass against oxygen mass fraction interpolated at their positions, comparing *High-* and *Low-Re* cases.

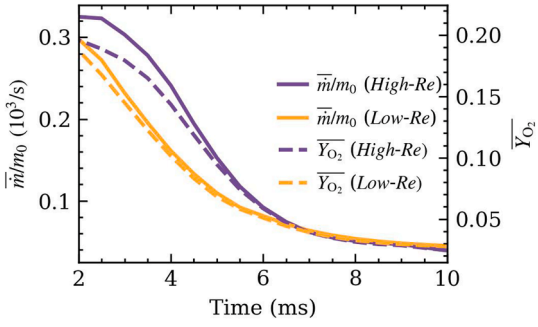

Fig. 13. Evolution of mean oxidation rate of the ignited particles normalized by their initial mass (left axis) and mean oxygen mass fraction interpolated at particle positions, comparing *High-* and *Low-Re* cases.

single-particle simulations to experimental data and a prior implementation, showing good agreement. A three-dimensional DNS cross-validation against the work by Luu et al. (2024a) confirmed the robustness and reproducibility of the datasets and included the first-time deterministic comparison of instantaneous realizations.

The influence of turbulence intensity on the ignition, oxidation, and burn-out characteristics of iron particles was investigated by extending the setup to a higher Reynolds number. It was found that the *High-Re* case exhibits the expected stronger turbulence, finer-scale structures, and faster growth of the shear- and mixing-layer. Clear streaks of particles following vortices are formed early on in *Low-Re* case, while in the

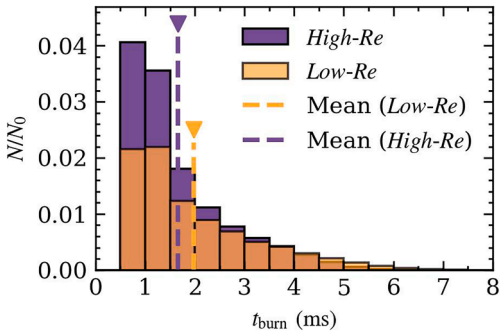

Fig. 14. Distribution of particle burn-time t_{burn}. Mean burn times are marked with dashed lines. The number of particles is normalized by the initial total number of particles.

High-Re these clusters were more dispersed and formed later than in *Low-Re*. The stronger turbulence in the *High-Re* case led to broader ignition zones and more sustained particle combustion at lower surrounding gas temperatures. The *High-Re* case exhibited higher ignition and conversion rates due to the broader reaction zone and enhanced oxygen entrainment caused by stronger turbulent mixing. The particle-scale oxidation behavior remained nearly identical between the two cases, indicating weak coupling between the gas-phase turbulence and individual particle combustion. Consequently, the enhanced combustion in the *High-Re* case is primarily attributed to increased oxygen availability rather than direct turbulence effects on the particle oxidation process.

CRediT authorship contribution statement

P. Ghofrani: Writing – original draft, Visualization, Validation, Software, Methodology, Investigation, Formal analysis, Data curation, Conceptualization. **T.D. Luu:** Writing – review & editing, Validation, Investigation, Data curation. **S.H. Tey:** Writing – original draft, Visualization, Validation, Software, Investigation. **O.T. Stein:** Writing – review & editing, Supervision, Formal analysis, Conceptualization. **A. Kempf:** Writing – review & editing, Supervision, Project administration, Funding acquisition, Formal analysis, Conceptualization.

Declaration of competing interest

The authors declare that they have no known competing financial interests or personal relationships that could have appeared to influence the work reported in this paper.

Acknowledgments

We gratefully acknowledge the funding received from the International Max Planck Research School for Sustainable Metallurgy (IMPRS SusMet). The authors also gratefully acknowledge the Gauss Centre for Supercomputing e.V. (www.gauss-centre.eu) for funding this project by providing computing time on the GCS Supercomputer SuperMUC-NG at Leibniz Supercomputing Centre (www.lrz.de). The KIT authors gratefully acknowledge the financial support by the Helmholtz Association of German Research Centres (HGF), within the research field Energy, program Materials and Technologies for the Energy Transition (MTET).

References

Bergthorson, J. M., Goroshin, S., Soo, M. J., Julien, P., Palecka, J., Frost, D. L., & Jarvis, D. J. (2015). Direct combustion of recyclable metal fuels for zero-carbon heat and power. *Applied Energy, 160*, 368–382. https://doi.org/10.1016/J.APENERGY.2015.09.037

Brosh, T., Patel, D., Wacks, D., & Chakraborty, N. (2015). Numerical investigation of localised forced ignition of pulverised coal particle-laden mixtures: A Direct Numerical Simulation (DNS) analysis. *Fuel, 145*, 50–62. https://doi.org/10.1016/J.FUEL.2014.12.006

Cen, L., Lyu, Z., Qian, Y., Zhong, W., & Lu, X. (2024). A detailed experimental and numerical study on the ignition temperature of single micron-sized spherical iron particles. *Combustion and Flame, 272*, 113909. https://doi.org/10.1016/j.combustflame.2024.113909

Cen, L., Qian, Y., & Lu, X. (2025). Surface morphology effects on ignition temperature of single micron-sized Iron particles. *Combustion and Flame, 277*, 114216. https://doi.org/10.1016/j.combustflame.2025.114216

Chen, G., Wang, H., Luo, K., & Fan, J. (2023). A DNS study of pulverized coal combustion in a hot turbulent environment: Effects of particle size, mass loading and preferential concentration. *Combustion and Flame, 254*, Article 112839. https://doi.org/10.1016/J.COMBUSTFLAME.2023.112839

Engelmann, L., Hasslberger, J., Baik, S. J., Klein, M., & Kempf, A. (2023). Direct numerical simulation of an unsteady wall-bounded turbulent flow configuration for the assessment of large-eddy simulation models. *Scientific Reports, 13*(1). https://doi.org/10.1038/s41598-023-37740-7

Fedoryk, M., Stelzner, B., Harth, S., & Trimis, D. (2023). Experimental investigation of the laminar burning velocity of iron-air flames in a tube burner. *Applications in Energy and Combustion Science, 13*, Article 100111. https://doi.org/10.1016/J.JAECS.2022.100111

Fiorina, B., Luu, T. P., Dillon, S., Mercier, R., Wang, P., Angelilli, L., Ciottoli, P. P., Hernández–Pérez, F. E., Valorani, M., Im, H. G., Massey, J. C., Li, Z., Chen, Z. X., Swaminathan, N., Popp, S., Hartl, S., Nicolai, H., Hasse, C., Dreizler, A., … Barlow, R. S. (2023). A joint numerical study of multi-regime turbulent combustion. *Applications in Energy and Combustion Science, 16*, Article 100221. https://doi.org/10.1016/J.JAECS.2023.100221

Hara, T., Muto, M., Kitano, T., Kurose, R., & Komori, S. (2015). Direct numerical simulation of a pulverized coal jet flame employing a global volatile matter reaction scheme based on detailed reaction mechanism. *Combustion and Flame, 162*(12), 4391–4407. https://doi.org/10.1016/J.COMBUSTFLAME.2015.07.027

Hazenberg, T., Braig, D., Fedoryk, M. A., Mich, J., Hagen, F. P., Harth, S. R., Stelzner, B., Scholtissek, A., Trimis, D., & Hasse, C. (2026). Analyzing iron dust bunsen flames using numerical simulations. *Fuel, 403*, Article 136094. https://doi.org/10.1016/J.FUEL.2025.136094

Hazenberg, T., & Van Oijen, J. A. (2021). Structures and burning velocities of flames in iron aerosols. *Proceedings of the Combustion Institute, 38*(3), 4383–4390. https://doi.org/10.1016/J.PROCI.2020.07.058

Hemamalini, S., Cuenot, B., van Oijen, J., & Mi, X. C. (2024). Numerical study probing the effects of preferential concentration on the combustion of iron particles in a mixing layer. *Proceedings of the Combustion Institute, 40*(1–4), Article 105617. https://doi.org/10.1016/J.PROCI.2024.105617

Julien, P., Whiteley, S., Goroshin, S., Soo, M. J., Frost, D. L., & Bergthorson, J. M. (2015). Flame structure and particle-combustion regimes in premixed methane–iron–air suspensions. *Proceedings of the Combustion Institute, 35*(2), 2431–2438. https://doi.org/10.1016/J.PROCI.2014.05.003

Kempf, A., Klein, M., & Janicka, J. (2005). Efficient Generation of Initial- and Inflow-Conditions for Transient Turbulent Flows in Arbitrary Geometries. *Flow Turbulence Combust, 74*, 67–84. https://doi.org/10.1007/s10494-005-3140-8

Klein, M., Sadiki, A., & Janicka, J. (2003). A digital filter based generation of inflow data for spatially developing direct numerical or large eddy simulations. *Journal of Computational Physics, 186*(2), 652–665. https://doi.org/10.1016/S0021-9991(03)00090-1

Krüger, J., Haugen, N. E. L., Mitra, D., & Løvås, T. (2017). The effect of turbulent clustering on particle reactivity. *Proceedings of the Combustion Institute, 36*(2), 2333–2340. https://doi.org/10.1016/J.PROCI.2016.06.187

Luu, T. D., Shamooni, A., Kronenburg, A., Braig, D., Mich, J., Nguyen, B. D., Scholtissek, A., Hasse, C., Thäter, G., Carbone, M., Frohnapfel, B., & Stein, O. T. (2024a). Carrier-phase DNS of ignition and combustion of iron particles in a turbulent mixing layer. *Flow, Turbulence and Combustion, 112*(4), 1083–1103. https://doi.org/10.1007/s10494-023-00526-y

Luu, T. D., Shamooni, A., Kronenburg, A., Braig, D., Mich, J., Nguyen, B. D., Scholtissek, A., Hasse, C., Thäter, G., Carbone, M., Frohnapfel, B., & Stein, O. T. (2024b). Carrier-phase DNS study of particle size distribution effects on iron particle ignition in a turbulent mixing layer. *Proceedings of the Combustion Institute, 40*(1–4), Article 105297. https://doi.org/10.1016/J.PROCI.2024.105297

Mich, J., Braig, D., Gustmann, T., Hasse, C., & Scholtissek, A. (2023). A comparison of mechanistic models for the combustion of iron microparticles and their application to polydisperse iron-air suspensions. *Combustion and Flame, 256*, Article 112949. https://doi.org/10.1016/J.COMBUSTFLAME.2023.112949

Neumann, J., Fradet, Q., Scholtissek, A., Dammel, F., Riedel, U., Dreizler, A., Hasse, C., & Stephan, P. (2024). Thermodynamic assessment of an iron-based circular energy economy for carbon-free power supply. *Applied Energy, 368*. https://doi.org/10.1016/j.apenergy.2024.123476

Nguyen, B. D., Scholtissek, A., Li, T., Ning, D., Stein, O. T., Dreizler, A., & Hasse, C. (2025). Nanoparticle formation in the boundary layer of burning iron microparticles: Modeling and simulation. *Chemical Engineering Journal, 507*, Article 160039. https://doi.org/10.1016/J.CEJ.2025.160039

Ning, D., Li, Y., Li, T., Böhm, B., & Dreizler, A. (2024). Size-resolved ignition temperatures of isolated iron microparticles. *Combustion and Flame, 270*, 113779. https://doi.org/10.1016/j.combustflame.2024.113779

Ning, D., Li, T., Mich, J., Scholtissek, A., Böhm, B., & Dreizler, A. (2023). Multi-stage oxidation of iron particles in a flame-generated hot laminar flow. *Combustion and Flame, 256*, Article 112950. https://doi.org/10.1016/J.COMBUSTFLAME.2023.112950

Ning, D., Shoshin, Y., van Oijen, J. A., Finotello, G., & de Goey, L. P. H. (2021). Burn time and combustion regime of laser-ignited single iron particle. *Combustion and Flame, 230*, Article 111424. https://doi.org/10.1016/J.COMBUSTFLAME.2021.111424

Ning, D., Shoshin, Y., van Oijen, J. A., Finotello, G., & de Goey, L. P. H. (2022). Critical temperature for nanoparticle cloud formation during combustion of single micron-sized iron particle. *Combustion and Flame, 244*, Article 112296. https://doi.org/10.1016/J.COMBUSTFLAME.2022.112296

Ning, D., Shoshin, Y., van Stiphout, M., van Oijen, J., Finotello, G., & de Goey, P. (2022). Temperature and phase transitions of laser-ignited single iron particle. *Combustion and Flame, 236*, Article 111801. https://doi.org/10.1016/J.COMBUSTFLAME.2021.111801

O'Brien, J., Urzay, J., Ihme, M., Moin, P., & Saghafian, A. (2014). Subgrid-scale backscatter in reacting and inert supersonic hydrogen–air turbulent mixing layers. *Journal of Fluid Mechanics, 743*, 554–584. https://doi.org/10.1017/jfm.2014.62

Panahi, A., Chang, D., Schiemann, M., Fujinawa, A., Mi, X., Bergthorson, J. M., & Levendis, Y. A. (2022). Combustion behavior of single iron particles-part I: An experimental study in a drop-tube furnace under high heating rates and high temperatures. *Applications in Energy and Combustion Science, 13*, 100097. https://doi.org/10.1016/j.jaecs.2022.100097

Ranz, W. E., & Marshall, W. R. (1952). Evaporation from drops. *Chemical Engineering Progress, 48*, 141–146.

Rieth, M., Kempf, A. M., Kronenburg, A., & Stein, O. T. (2018). Carrier-phase DNS of pulverized coal particle ignition and volatile burning in a turbulent mixing layer. *Fuel, 212*, 364–374. https://doi.org/10.1016/J.FUEL.2017.09.096

Shamooni, A., Debiagi, P., Wang, B., Luu, T. D., Stein, O. T., Kronenburg, A., Bagheri, G., Stagni, A., Frassoldati, A., Faravelli, T., Kempf, A. M., Wen, X., & Hasse, C. (2021). Carrier-phase DNS of detailed NOx formation in early-stage pulverized coal combustion with fuel-bound nitrogen. *Fuel, 291*, Article 119998. https://doi.org/10.1016/J.FUEL.2020.119998

Soo, M., Goroshin, S., Bergthorson, J. M., & Frost, D. L. (2015). Reaction of a particle suspension in a rapidly-heated oxidizing gas. *Propellants, Explosives, Pyrotechnics, 40*(4). https://doi.org/10.1002/prep.201400269

Steffens, P., Hebel, J., Braig, D., Vahl, A., Berkel, L. L., Schary, S., Nicolai, H., Scholtissek, A., Dreizler, A., Böhm, B., & Hasse, C. (2025). Exploring turbulent methane-assisted iron dust combustion: A combined experimental and numerical study of a 47 kWth lab-scale combustor. *Fuel, 392*, Article 135205. https://doi.org/10.1016/J.FUEL.2025.135205

Thäter, G., Carbone, M., Luu, T. D., Stein, O. T., & Frohnapfel, B. (2024). The influence of clustering in homogeneous isotropic turbulence on the ignition behavior of iron particles. *Proceedings of the Combustion Institute, 40*(1–4), Article 105348. https://doi.org/10.1016/J.PROCI.2024.105348

Thijs, L. C., Ning, D., Shoshin, Y. S., Hazenberg, T., Mi, X. C., van Oijen, J. A., & de Goey, P. (2024). Temperature evolution of laser-ignited micrometric iron particles: A comprehensive experimental data set and numerical assessment of laser heating impact. *Applications in Energy and Combustion Science, 19*, Article 100284. https://doi.org/10.1016/J.JAECS.2024.100284

Thijs, L. C., van Gool, C. E. A. G., Ramaekers, W. J. S., Kuerten, J. G. M., van Oijen, J. A., & de Goey, L. P. H. (2022). Improvement of heat- and mass transfer modeling for single iron particles combustion using resolved simulations. https://doi.org/10.1080/00102202.2022.2089030.

Thijs, L. C., van Gool, C. E. A. G., Ramaekers, W. J. S., van Oijen, J. A., & de Goey, L. P. H. (2023). Resolved simulations of single iron particle combustion and the release of nano-particles. *Proceedings of the Combustion Institute, 39*(3), 3551–3559. https://doi.org/10.1016/J.PROCI.2022.07.044

Vance, F. H., Scholtissek, A., Nicolai, H., & Hasse, C. (2023). Flame propagation modes for iron particle clusters in air — Part I: Transition from continuous to discrete propagation mode under weak convection effects. *Combustion and Flame, 260*, 113265. https://doi.org/10.1016/j.combustflame.2023.113265

Vance, F. H., Scholtissek, A., Nicolai, H., & Hasse, C. (2025). Propagation of iron dust flames near a wall using boundary-layer resolved simulations. *Fuel, 401*, 135867. https://doi.org/10.1016/j.fuel.2025.135867

Wang, B., Shamooni, A., Stein, O. T., Kronenburg, A., Kempf, A. M., Debiagi, P., & Hasse, C. (2021). Investigation of turbulent pulverized solid fuel combustion with detailed homogeneous and heterogeneous kinetics. *Energy and Fuels, 35*(9), 7077–7091. https://doi.org/10.1021/acs.energyfuels.0c03479